Interfacial reconstruction and superconductivity in cuprate–manganite multilayers of $YBa_2Cu_3O_{7-}$ and $Pr_{0.68}Ca_{0.32}MnO_3$

2012 New J. Phys. 14 093009

(http://iopscience.iop.org/1367-2630/14/9/093009)

New Journal of Physics
The open-access journal for physics

Interfacial reconstruction and superconductivity in cuprate–manganite multilayers of $YBa_2Cu_3O_{7-\delta}$ and $Pr_{0.68}Ca_{0.32}MnO_3$

J Norpoth[1,5], D Su[2], H Inada[3], S Sievers[4], Y Zhu[2] and Ch Jooss[1]

[1] Institute of Materials Physics, University of Goettingen, Friedrich-Hund-Platz 1, 37077 Goettingen, Germany
[2] Brookhaven National Laboratory, Upton, NY 11973, USA
[3] Hitachi High-Technologies Corp., Ibaraki, Japan
[4] Physikalisch-Technische Bundesanstalt, Bundesallee 100, 38116 Braunschweig, Germany
E-mail: norpoth@ump.gwdg.de

New Journal of Physics **14** (2012) 093009 (15pp)
Received 13 April 2012
Published 7 September 2012
Online at http://www.njp.org/
doi:10.1088/1367-2630/14/9/093009

Abstract. Interfacial reconstruction in multilayers of $YBa_2Cu_3O_{7-\delta}$ and $Pr_{0.68}Ca_{0.32}MnO_3$ and its impact on superconducting properties is investigated by means of electron energy-loss spectroscopy and dc electrical transport measurements. Massive underdoping of the cuprate is found by both electron transfer from the manganite and interfacial oxygen depletion, presumably as an adaptation to compressive epitaxial stress. The decrease of the optimally doped volume becomes evident from a distinct suppression of the superconducting transition temperature. This doping effect is stronger than the impact of a competing ferromagnetic order parameter reported for similar multilayer samples with spin-polarized manganites.

[5] Author to whom any correspondence should be addressed.

Contents

1. Introduction

The versatile structural and electronic properties of perovskite oxides provide manifold degrees of freedom for interfacial reconstruction schemes: octahedral tiltings to balance lattice mismatch and strain [1, 2], mixed transition-metal cation valence to compensate for polar discontinuities and the creation or ordering of oxygen vacancies as an alternative to compositional roughening [3, 4]. Much attention has been paid to novel electronic and magnetic phases emerging in the vicinity of such interfaces between perovskites, further enriching their already complex phase diagrams [5–10]. The integration of the cuprate superconductor $YBa_2Cu_3O_{7-\delta}$ (YBCO) into thin film superlattices or heterostructures with other perovskites was the subject of a number of studies focusing on the implications for the superconducting properties. Short-scale suppression of the superconducting transition temperature was found to be related to interlayer decoupling of coherence between CuO_2 planes in ultrathin superlattices [11] and to variations in intracell distances by means of epitaxial strain [12, 13]. Proximity to ferromagnetic manganites, e.g. $La_{0.7}Ca_{0.3}MnO_3$, yields additional spin injection effects on a 10 nm scale [14, 15] and conversely, a suppression of the magnetization in the manganite by stationary charge transfer across the interface [16, 17]. More recently, observations of inverse spin-switch behaviour [18, 19] have been discussed in terms of interfacial magnetic coupling [20, 21].

In this paper, we provide an example where the oxygen degree of freedom dominates the superconducting properties of YBCO in a superlattice. In multilayers with antiferromagnetic $Pr_{0.68}Ca_{0.32}MnO_3$ (PCMO), electron energy-loss spectroscopy (EELS) reveals that a combined interfacial reconstruction composed of short-scale Ca interdiffusion, charge transfer and especially intrinsic oxygen depletion lies at the bottom of a strong suppression of superconductivity.

2. Experimental details

Various multilayer samples, $[YBCO_{t_Y}/PCMO_{t_P}]_N$ with $t_Y = 6$–45 nm, $t_P = 8$–12 nm and $N = 3$–12, were grown epitaxially on polished $(LaAlO_3)_{0.3}$–$(Sr_2AlTaO_6)_{0.7}(100)$ or $SrTiO_3(100)$ substrates by pulsed laser deposition (PLD) from stoichiometric targets. Process parameters

were a substrate temperature of 770 °C and an oxygen partial pressure of 0.4 (0.2) mbar during deposition of YBCO (PCMO). The pulsed KrF excimer laser operated at a 5 Hz rate with a fluence of 1.5 J cm^{-2} at the targets, providing deposition rates of 45 (20) nm min^{-1} for YBCO (PCMO). Post-deposition cooling was performed in 900 mbar of pure oxygen at a rate of 15 °C min^{-1} with a 1–2 h oxygen loading stage at 400 °C. The multilayer stacking sequence always starts with a PCMO buffer layer, also the top layer typically consists of PCMO to prevent the rather susceptible YBCO from deterioration.

Electron-transparent lamellae for cross-section analysis were prepared with a focused ion beam and subsequent low-angle (<10°), low-energy (2 keV) Ar ion milling. In order to avoid edge formation or intermixing at the YBCO/PCMO interfaces, the Ar milling was performed so that the azimuthal projection of the incident beam on the cross-section was parallel to the layers.

As references for the determination of cation valence from spectroscopic data, additional electron-transparent lamellae were taken from samples of $PrMnO_3$, $CaMnO_3$ and $Pr_{0.5}Ca_{0.5}MnO_3$. While the former are epitaxial thin film samples prepared by ion beam sputtering and PLD, respectively, the latter is polycrystalline target material. A reference thin film of oxygen-deficit YBCO was prepared by PLD with post-deposition cooling at an oxygen partial pressure of only 0.01 mbar.

Structure analysis includes x-ray diffraction (XRD), (scanning) transmission electron microscopy ((S)TEM) and EELS. STEM and EELS analyses were performed with Brookhaven's Hitachi HD-2700 STEM with a C_s-corrected probe [22]. Therein, high-angle annular dark field (HAADF) imaging comprised collection angles of 53–280 mrad, and for EELS, a spectrometer collection semi-angle of 20 or 24 mrad at a convergence semi-angle of 28 mrad was used.

Electrical transport measurements were made in the van-der-Pauw setup with a constant test current of 0.5 mA. To this end, 1×1 mm^2 Au contacts were sputter coated at each corner of the 5×10 mm^2 samples.

Magnetization measurements were made in a superconducting quantum interference device magnetometer with in-plane magnetic fields applied along a substrate edge.

3. Results and discussion

3.1. Microstructure and chemical reconstruction of the interface

XRD and selected area electron diffraction reveal epitaxial growth with YBCO grown in the $\langle 00l \rangle$ direction (notation in space group Pmmm (no. 47)) and PCMO exhibiting twins with $\langle hh0 \rangle$ and $\langle 00l \rangle$ out-of-plane orientation, respectively (Pbnm (no. 62)), see the inset of figure 1(a). The corresponding epitaxial in-plane relations read YBCO$\langle h00 \rangle \| $PCMO$\langle 00l \rangle$ or PCMO$\langle hh0 \rangle$, respectively. Figure 1(a) shows a representative cross-section of a multilayer sample, here $[YBCO_{12nm}/PCMO_{12nm}]_4$. The PCMO layer labelled *P* exhibits a columnar $\langle 00l \rangle$ nano-twin in $\langle hh0 \rangle$ surroundings. Stacking faults, antiphase boundaries and, to a minor extent, epitaxial yttria (Y_2O_3) nano-particles are found in the YBCO layers, compare, e.g., [23, 24]. The microstructural features of the YBCO are also reflected in an asymmetry concerning the layer stacking sequence: PCMO grows on rather irregular YBCO surfaces (termed PonY interface in the following), but in turn mediates this roughness and provides a smooth buffer

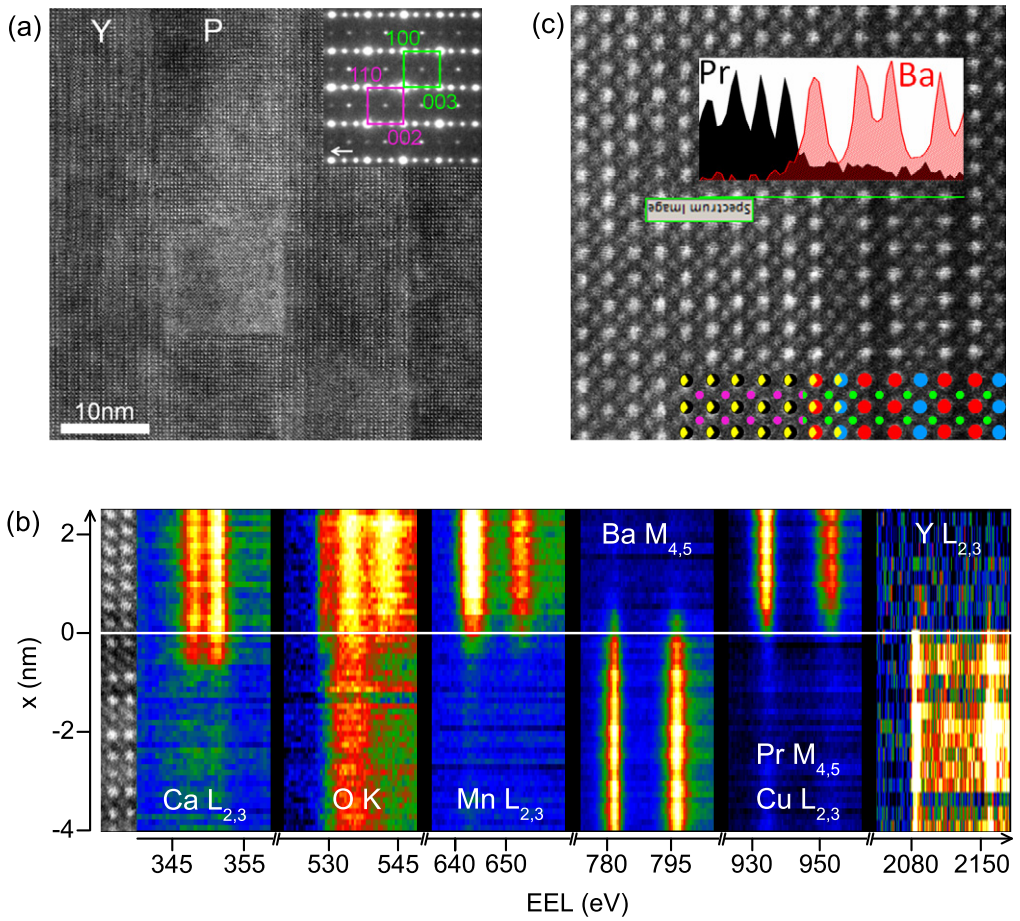

Figure 1. Atomic structure of the YBCO/PCMO interface, the sample $[YBCO_{12nm}/PCMO_{12nm}]_4$. (a) HAADF cross-section image with alternating layers of YBCO (Y) and PCMO (P). Inset: the corresponding diffraction pattern with [010] and $[1\bar{1}0]$ zone axes in YBCO (green) and PCMO (pink label), respectively. The squares correspond to the reciprocal-space equivalent of the perovskite pseudo-cubic unit cell. The arrow indicates the substrate normal. (b) Colour-coded intensity of core-loss edges simultaneously acquired in an EELS line scan across a YonP-interface (except Y $L_{2,3}$, which required a separate detector range and was acquired subsequently). The B-cation site between Ba and Pr is defined as the interface position ($x = 0$) and is indicated by the horizontal white line. The leftmost panel displays the corresponding HAADF image. (c) HAADF image of a YonP-interface at an ultrathin lamella position ($t/\lambda < 0.2$), the same zone-axis as in (a). Inset: integrated intensity of Pr and Ba $M_{4,5}$ ELNES along the line scan given by the green line. Note that the Pr signal is overlaid with the Cu $L_{2,3}$ edge. At the bottom, the interfacial atomic structure model based on the EELS data is illustrated by cation columns colour-coded as follows: Pr black, Ca yellow, Mn pink, Y blue, Ba red and Cu green.

for the subsequent YBCO layer (YonP interface). The remaining half unit cell steps and twin boundaries at the PCMO surface induce planar defects in the YBCO. The interfaces between all layers are free of misfit dislocations.

The chemical composition of the interfaces was investigated by means of EELS line scans. Figure 1(b) shows the spatial evolution of energy-loss near-edge structures (ELNES) from all relevant core-loss edges across a YonP interface. By fitting error-function profiles to the integrated intensities of each ELNES, we deduced the following atomic model, which is also illustrated in figure 1(c). The interface is located between perovskite A-site layers of (nominal) $Pr_{0.68}Ca_{0.32}$–O and Ba–O. The very interface, defined as $x = 0$ in the following, is a perovskite B-site with unresolved composite character of Mn–O_2 and Cu–O. The exact determination of Cu contributions is hindered by the low signal-to-noise ratio of the Cu $L_{2,3}$ edge and its complete overlap with Pr $M_{4,5}$. Multiple linear least-squares fits of the interfacial O K ELNES with two reference spectra from YBCO and PCMO bulk (see figure 3(a)) support a mixed Mn/Cu scenario. A robust feature of the YonP-interface is a distinctive short-scale diffusion of Ca into the first YBCO unit cell. The inflection point of the corresponding error function profile is located at $x = -0.6$ nm, i.e. at the first Y-site. We will further discuss the implications of this observation below.

The morphological asymmetry of the interfaces with respect to the layer stacking sequence is also reflected in the appropriate chemical profiles. In contrast to the abrupt YonP-interfaces, PonY-interfaces are characterized by a narrow interdiffusion zone, especially concerning the heavy A-site cations, i.e. Pr and Ba. The corresponding error function profiles provide an interdiffusion zone width of 2–3 nm (indicating a decrease of the element concentrations from 90 to 10%).

3.2. Interfacial charge transfer and electronic reconstruction

An important factor for the electronic and magnetic properties of the interface-near region is given by the transfer of charge across the interface, i.e. mutual doping of adjacent layers. Access to the local doping level is provided by the ELNES of core-loss edges, since they probe transitions to the first unoccupied states above the Fermi level. In particular, the O K edge (1s→ 2p transition) can be interpreted as the site- and symmetry-projected density-of-states due to the strong screening of the remaining core-hole [25]. Figure 2 shows the doping trends in the O K ELNES of PCMO and YBCO, realized by A-site substitution and varying oxygen content, respectively. The different spectral features arise from covalent mixing of O 2p states with the various A- and B-site metal orbitals, namely transition metal 3d (label K_1), A-site metals Pr 4f5d, Ca 3d, Ba 4f5d, Y 4d (K_2) and higher sp orbitals (K_3) [26–28]. The shape, position and weight of feature K_1 are affected by the 3d band filling and the local symmetry [27, 29, 30], and it thus represents a useful probe of the transition metal valence [31–33].

Focusing on the manganite, further information on the Mn valence is provided by the Mn $L_{2,3}$ ELNES (figure 2(a)), which is dominated by excitations from (spin–orbit split) 2p→ 3d and which is subject to multiplet effects due to strong wavefunction overlap between the final state and the core-hole [34]. Both the L_3/L_2 branching ratio and Mn L_3–O K_1 distance have been used for Mn valence determination [33, 35, 36]. In order to extract systematic variations of these valence markers in $Pr_{1-y}Ca_yMnO_3$, we fitted double Gaussians to the O K_1 and K_2 ELNES features (triple for $y = 1$) and double Gaussians to Mn $L_{2,3}$. To this end, in addition to background subtraction, Mn $L_{2,3}$ spectra have been corrected for post-edge continuum contributions according to the scheme proposed by Varela *et al* [33].

The precise doping level of the different YBCO samples displayed in figure 2(b) is undetermined. We are therefore restricted to the mere qualitative correlation between the

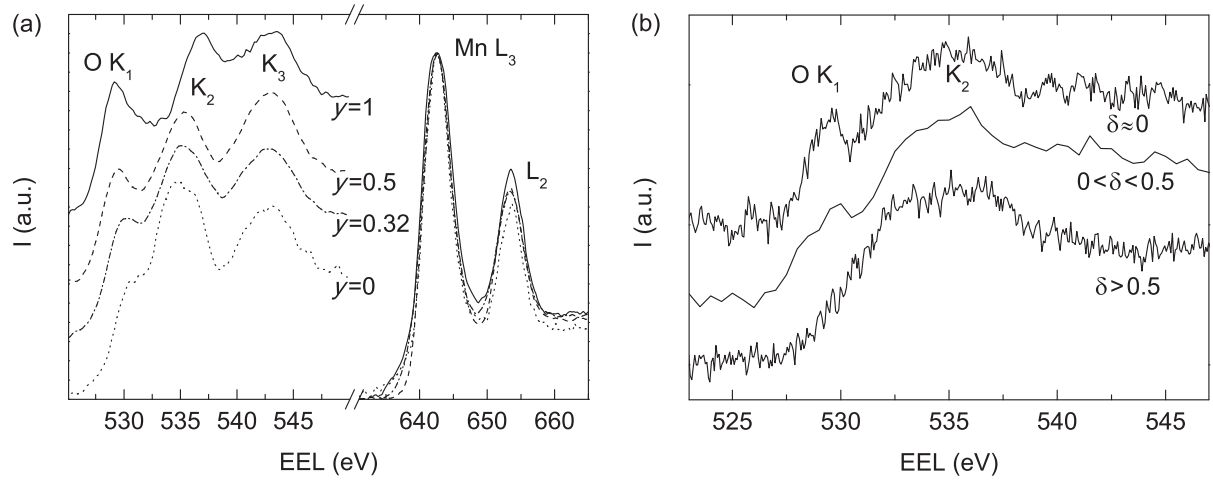

Figure 2. Doping trends in ELNES. (a) Background-subtracted O K and Mn $L_{2,3}$ edges of $Pr_{1-y}Ca_yMnO_3$ and (b) O K of $YBa_2Cu_3O_{7-\delta}$. In (b), heavy oxygen depletion ($\delta > 0.5$) was achieved by artificial electron beam damage in the STEM. Reference to the labelling of spectral features is given in the text. Spectra are aligned to match the joint position and height of features O K_3, Mn L_3 (a) and O K_2 (b), respectively; O K spectra are offset vertically. The data each represent average values of several point spectra in order to increase the signal-to-noise ratio.

decrease of O K_1 intensity with oxygen deficit or hole depletion, respectively. According to [31, 37], the total decline of a distinct K_1 peak occurs not until $\delta > 0.6$.

The spatial evolution of O K_1 spectral weight across an embedded YBCO layer is shown in figure 3(b). A strong suppression is obvious in the vicinity of the interfaces to PCMO with uniform recovery towards the layer centre. Comparison with the corresponding values from the reference spectra in figure 2(b) points to a massive hole depletion in a zone extending roughly 3 nm from the respective interfaces. An associated electron depletion on the PCMO side of the interface is displayed in figures 3(c)–(e): all markers indicate a mid-layer Mn valence corresponding to the nominal Ca-doping level ($V_{Mn} = +3.32$) within error bars and an increase by roughly +0.2 within 1 nm from the interface.

The observed electron transfer from PCMO to YBCO corresponds to the difference in the work functions of the materials, namely $\phi_{PCMO} = 4.89$ eV [38] and $\phi_{YBCO} = 5$–6 eV ([39] and references therein). Considering the YBCO/PCMO interface as a p–p heterojunction, the width of the space charge layer around the interface can be estimated from $w = \sqrt{2\epsilon_0\epsilon_Y\epsilon_P V_{bi}(n_Y + n_P)^2/(e n_Y n_P(\epsilon_Y n_Y + \epsilon_P n_P))}$ [40]. Therein, the charge carrier densities of doped holes in the e_g-band of PCMO (0.32/Mn) and in CuO_2 layers of optimally doped YBCO (0.5/Cu) both amount to $n_{Y,P} \sim 5 \times 10^{21}$ cm^{-3}; the static dielectric constants at room temperature are $\epsilon_Y \sim 100$ [41] and $\epsilon_P = 30$ [42], respectively. Built-in voltages in the range $V_{bi} = 0.1$–1.1 V (the work function difference) then yield total space charge layer widths of $w = 0.5$–1.5 nm. These values roughly correspond to the experimentally observed 1 nm zone on the PCMO side of the junction, but they are not in line with the more extended hole depleted region in the YBCO. An additional effect stems from the short-scale Ca interdiffusion that changes the Ca^{2+}/Pr^{3+} ratio at the interface and therefore contributes to the local increase of

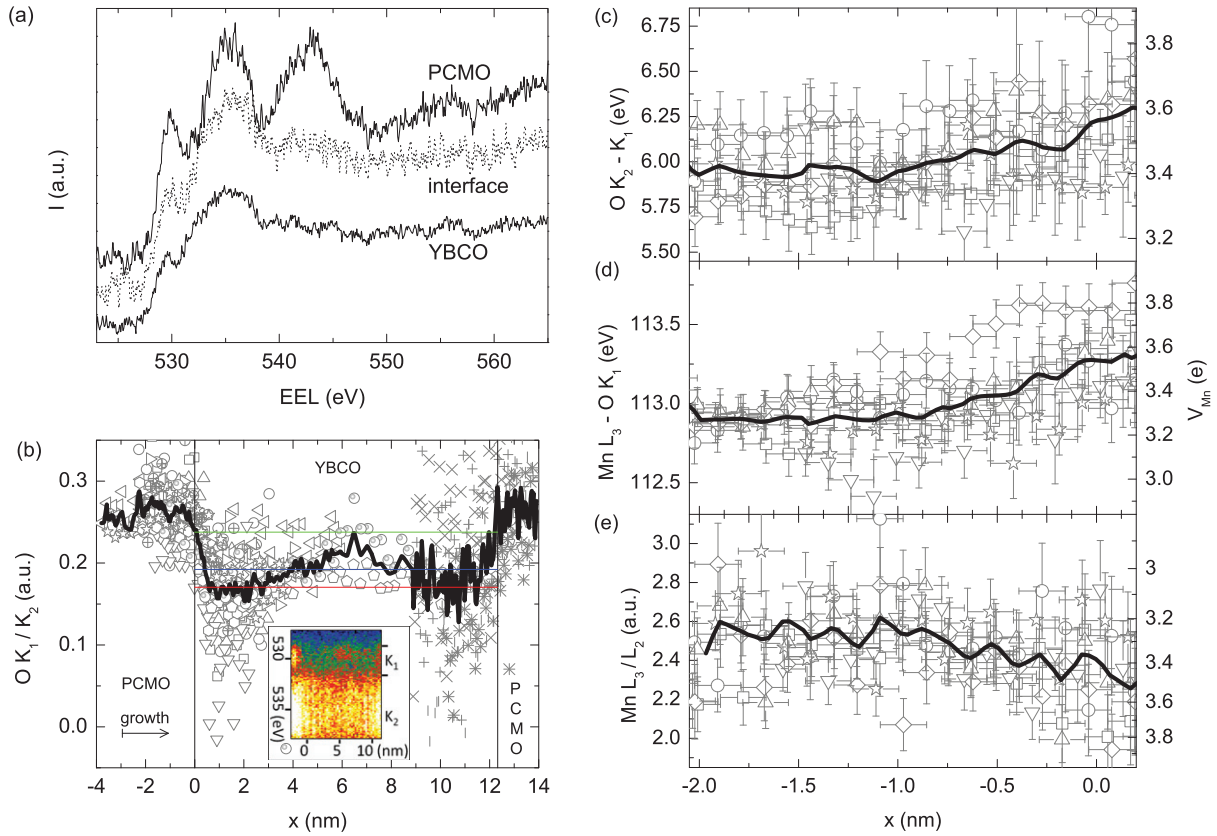

Figure 3. Charge carrier reconstruction in the YBCO/PCMO multilayer, the sample $[YBCO_{12nm}/PCMO_{12nm}]_4$. (a) O K ELNES at selected positions around a YonP-interface. Labels PCMO and YBCO denote averaged spectra from the central part of the respective layers, *interface* indicates the average of two point spectra acquired at distances $x = \pm 0.15$ nm around the corresponding interface. Spectra are offset vertically. (b) O K_1/K_2 doping marker evolution in the PCMO/YBCO/PCMO multilayer section. Symbols represent data from individual EELS line scans; the black line is their average. The spectral weight of $K_1(K_2)$ is determined by integrating its intensity in a 3 (7.5) eV window. Vertical lines display the interface positions; horizontal lines represent the respective K_1/K_2 ratios of the reference spectra in figure 2(b) ($\delta \approx 0$, green; $0 < \delta < 0.5$, blue; $\delta > 0.5$, red). The multilayer growth direction is indicated by the arrow. Inset: colour-coded O K ELNES intensity of a selected line scan (compare the denoted symbol). (c)–(e) Valence marker evolution and the corresponding Mn valence V_{Mn} in PCMO as a function of the distance to a YonP-interface at $x = 0$. Symbols represent data from individual EELS line scans, black lines are their average. The position and intensity of the denoted spectral features stem from multiple-Gaussian fits to the respective ELNES (see text). In order to increase the signal-to-noise ratio, three successive point spectra of the line scans are averaged prior to fitting, as represented by the horizontal error bars; vertical error bars indicate standard errors from fitting.

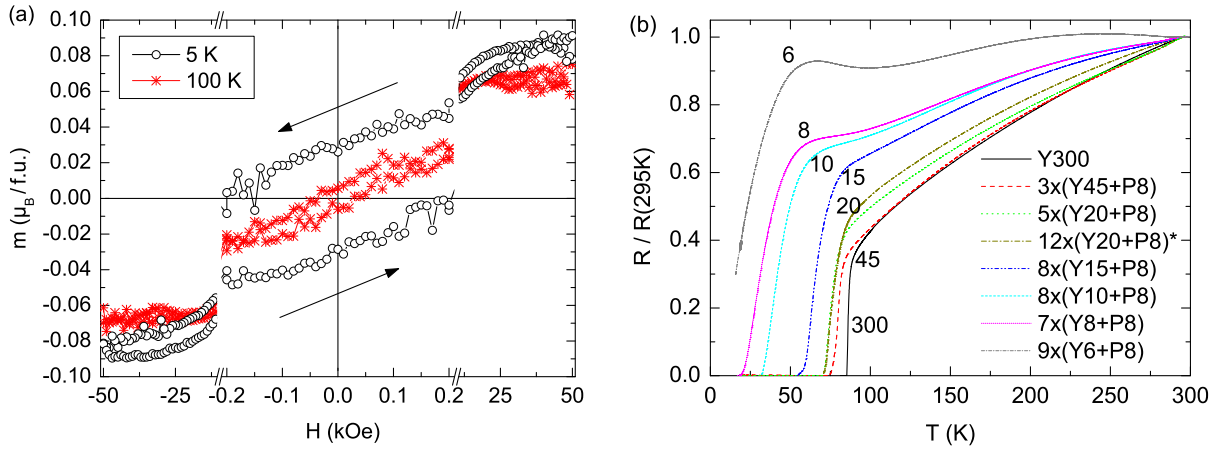

Figure 4. (a) In-plane magnetic moment m of PCMO in the sample $[YBCO_{20nm}/PCMO_{8nm}]_{12}$ at selected temperatures (in Bohr magnetons per formula unit). Data have been corrected for the diamagnetic contributions of the substrate and YBCO. Arrows indicate the directions of the magnetic field sweep; the initial curves are not shown. (b) Normalized resistance of various YBCO/PCMO multilayer samples (The number following Y (P) represents the thickness of the individual YBCO (PCMO) layers in nm. The respective YBCO thickness is additionally indicated next to the curves.). All the samples are deposited on an 8 nm PCMO buffer layer, except Y300, which is on 100 nm buffer. The sample labelled with an asterisk was subjected to an extended *in-situ* oxygen loading stage (16 h at 400 °C and 900 mbar O_2).

the Mn valence. In YBCO, the aliovalent substitution of Y^{3+} by Ca^{2+} nominally yields hole doping, thus counteracting the electron transfer from the PCMO, but this effect is known to be compensated for by a concomitant oxygen loss [43]. The long-range hole depleted region in the YBCO side of the junction is most likely caused by an appropriate oxygen deficit. Further evidence for this assumption is provided by the electrical transport data presented in the following subsection.

3.3. Suppression of the superconducting transition temperature

Electrical transport and magnetization have been probed in a sample batch of multilayers with varying YBCO single-layer thickness at a constant PCMO single-layer thickness of 8 nm. We first discuss the magnetic properties of the PCMO layers in order to estimate the potential impact on superconductivity. $Pr_{1-y}Ca_yMnO_3$ in the doping range $0.3 \leqslant y \leqslant 0.5$ exhibits antiferromagnetic ordering below $T_N \approx 150$ K, typically incorporating a minor fraction of ferromagnetic clusters [44–47]. The magnetization curves from our multilayer samples (see figure 4(a) for a representative example) show a weak magnetic moment ($m = 0.09\,\mu_B$ per formula unit at 5 K in saturation), which is suppressed by a factor of ∼20 compared to single-layer values reported in the literature [48]. An equally strong suppression is reported in the literature for comparable multilayer structures of YBCO and $La_{0.7}Ca_{0.3}MnO_3$ (LCMO) [17, 49]; furthermore, magnetically dead layers of 3–5 nm are observed in ultra-thin single layers of LCMO and $La_{0.7}Sr_{0.3}MnO_3$ (LSMO) on various substrates [50–53]. We conclude

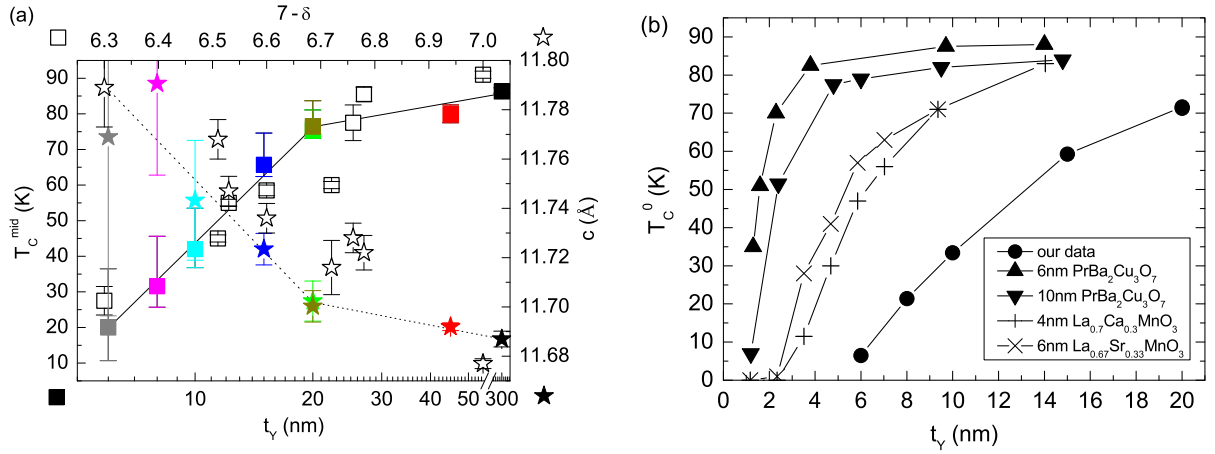

Figure 5. (a) A comparison of our multilayer data (filled symbols) with the work of Cava *et al* [54] on oxygen-doping trends in YBCO bulk samples (open symbols). The superconducting transition temperature T_C^{mid} (squares; error bars indicate 90–10% resistive transition width with the midpoint marked by the symbol) and out-of-plane lattice constant c of YBCO (stars) as a function of the individual YBCO layer thickness t_Y and the bulk sample oxygen content $7-\delta$, respectively. Colour code according to figure 4(b). The straight lines are a guide to the eye, intended to visualize the trends in our data. (b) Zero-resistance temperature T_C^0 of our samples compared with the corresponding data from the literature on YBCO multilayers with non-magnetic $PrBa_2Cu_3O_7$ [11, 12] and ferromagnetic manganites [49, 57], respectively.

that the low spin polarization in PCMO has only insignificant implications for superconducting properties of YBCO.

The dc electrical resistance is displayed in figure 4(b). In all samples, it is dominated by the YBCO portion as reflected by the essentially positive dR/dT and the superconducting phase transition. The critical temperature of a reference sample with a 300 nm YBCO single layer on a 100 nm PCMO buffer (Y300) amounts to $T_C^{mid} = 86.5$ K (1.5 K transition width), which is slightly reduced compared with (90 ± 0.5) K for a 300 nm YBCO single layer deposited directly on a $SrTiO_3$ substrate under the same conditions. The resistivity at room temperature increases from 0.5 mΩ cm in Y300 to 3.5 mΩ cm in $[YBCO_{6nm}/PCMO_{8nm}]_9$. This resistivity variation as well as the deviations from a constant dR/dT slope above T_C are consistent with an enhanced oxygen deficit in the thinner YBCO layers [54]. A direct comparison with the literature data from systematic oxygen doping of polycrystalline samples is given in figure 5(a). Therein we provide evidence that the YBCO layer thickness t_Y in our multilayers corresponds to an effective oxygen deficit $\delta^{eff}(t_Y)$, since both the critical temperature and the out-of-plane lattice constant, determined from XRD, exhibit roughly the same relation between t_Y and δ of the reference samples. Accordingly, the YBCO layers in $[YBCO_{6nm}/PCMO_{8nm}]_9$ are subject to a heavy deficit, $\delta^{eff}(6nm) \approx 0.7$, which is consistent with (merging) interfacial 3 nm zones of strong O K_1 suppression (recall the EELS profiles in figure 3(b)).

We want to point out that for several reasons, such an oxygen deficit in YBCO layers is not related to insufficient post-deposition oxygen loading (1–2 h at 400 °C and 900 mbar O_2). The

oxygen diffusion coefficient along $\langle 00l \rangle$ bulk YBCO at 400 °C amounts to 10^{-16} cm^2 s^{-1} [55], whereas De Souza and Kilner [56] indicate a corresponding coefficient of only $\sim 10^{-23}$ cm^2 s^{-1} in the manganite. However, independent of the incorporation of PCMO layers that possibly hinder oxygen diffusion along the out-of-plane direction, oxygen loading of YBCO essentially takes place via the lateral surfaces of the multilayer stack: the oxygen diffusion coefficient in the (a, b)-plane is known to be up to 10^6 times faster than along $\langle 00l \rangle$ [55] and therefore dominates the loading process, since the ratio of normal to lateral sample dimensions is equal to only $\sim 100\,\text{nm}/1\,\text{mm} = 10^{-4}$. Consistent with this, extending the post-deposition oxygen loading time to 16 h has no impact on either the critical temperature or the out-of-plane lattice constant (compare the samples $[YBCO_{20nm}/PCMO_{8nm}]_5$ and $[YBCO_{20nm}/PCMO_{8nm}]_{12}$ in figures 4(b) and 5(a)). Furthermore, the triangular shape of the doping profile in individual YBCO layers (figure 3(b)) contradicts an overall top–bottom gradient in the oxygen level.

Figure 5(b) gives a comparison with T_C values from the literature data for related multilayer samples of YBCO with non-magnetic $PrBa_2Cu_3O_7$ (PBCO) and ferromagnetic manganites, respectively. While superconductivity prevails even in single unit cell YBCO layers in the former, the competition between superconducting and ferromagnetic order parameters leads to a T_C suppression in the YBCO/LCMO and YBCO/LSMO systems. No evidence for interface-near oxygen depletion was reported for any of these reference systems; in fact, contrary to our samples, the out-of-plane lattice constant of YBCO was found to shrink when the layer thickness is decreased [12, 57]. Compared with the impact of magnetic coupling and spin polarization, the pure effect of hole underdoping due to the oxygen deficit in YBCO/PCMO predominates. However, the aforementioned, size-induced reduction of spin polarization of the manganite layers in thin heterostructures [17, 49] poses a restriction on this comparison. Indeed, the impact of a fully spin-polarized 50 nm LCMO layer on the T_C of a YBCO single layer proves to be heavier than the suppression seen in our multilayer samples [15].

We argue that the PCMO imparts compressive in-plane stress on the YBCO, resulting in the observed out-of-plane expansion and oxygen vacancy formation. The compensation of interfacial stress from lattice mismatch or differences in thermal expansion behaviour has already been discussed as a possible source of oxygen deficit or disorder in YBCO heterostructures [58]. Evidence for this is provided by geometric phase analysis (GPA) [59] of appropriate high-resolution TEM images. Analysis of the interface between the substrate and the PCMO buffer layer indicates full stress relaxation within the first 5–10 nm of the manganite. Taking the equilibrium lattice constant of the substrate as the reference yields a pseudo-cubic in-plane lattice constant of $a_{pc} = 0.383$ nm in the relaxed portion of the PCMO buffer. Comparison with the average equilibrium in-plane lattice constant of fully oxygenated YBCO $\langle a \rangle = (a+b)/2 = 0.386$ nm ($a = 0.382$ nm and $b = 0.389$ nm, taken from pure phase powder samples [60]) indeed points to compressive stress in the on-growing cuprate layer, at least during the early growth stage. The formation of oxygen vacancies in the Cu–O chains of the YBCO, thus shortening the b parameter, is a plausible mechanism to release this stress. The GPA map in figure 6 reveals a very inhomogeneous strain state in the YBCO, which is on average positive compared to the underlying PCMO buffer. The thin PCMO layer sandwiched between YBCO tends to respond to this tensile strain, which is an expression of its lower elastic modulus $E_{PCMO} < 100$ [61] compared to $E_{YBCO} \approx 200$ [62]. The average strain of the two YBCO layers in figure 6 with respect to the PCMO buffer is $\Delta\epsilon_{ip} \approx +0.6\%$. This value corresponds to $\langle a \rangle = 0.385$ nm, i.e. to a slightly compressive strain compared to the equilibrium

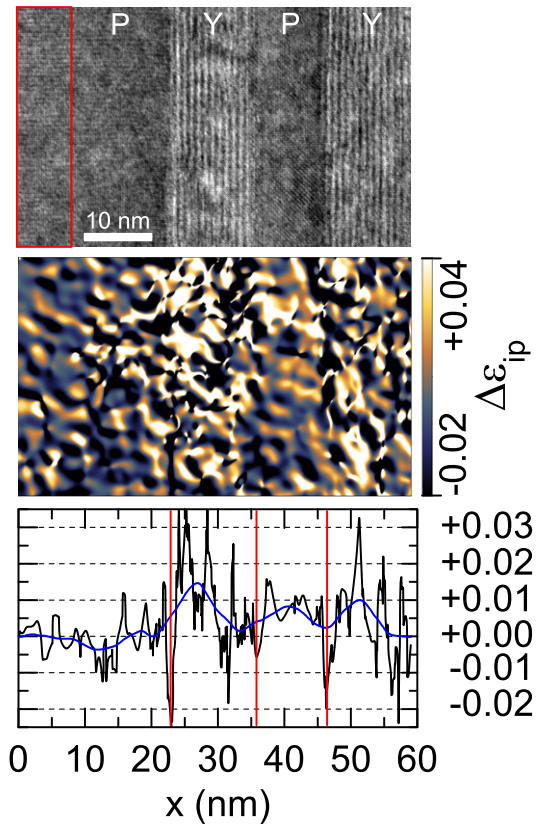

Figure 6. In-plane strain from GPA analysis, the sample $[YBCO_{12nm}/PCMO_{12nm}]_4$ on a 30 nm PCMO buffer layer. (a) Bright-field TEM cross-section image in the [010] and $[1\bar{1}0]$ zone axes in YBCO (Y) and PCMO (P), respectively. The wide leftmost layer is the top of the PCMO buffer. (b) The corresponding in-plane strain $\Delta\epsilon_{ip}$ map with respect to the relaxed PCMO buffer indicated as a red rectangle in (a). (c) Column-wise average of $\Delta\epsilon_{ip}$ (black line, adjacent-average smoothed profile in blue). The red vertical lines display the interface positions.

YBCO structure. In contrast, tensile stress/strain in YBCO presumably prevails in multilayer samples with ferromagnetic manganites of higher tolerance factor, LSMO ($a_{pc} = 0.390$ nm [63]) and LCMO (0.387 nm [63]), and also on PBCO (0.390 nm [64]).

Another hint of adaptation to a compressively strained environment is the incorporation of Ca into the first YBCO unit cell on top of PCMO (recall the chemical reconstruction in figure 1): Ca is known for its high solubility limit of 30% on Y-sites in YBCO [65], but substitutes for Ba only under compression [66, 67].

We conclude that subtle details of the interfacial reconstruction may govern the doping level and thus the superconducting transport properties of cuprates in cuprate/manganite superlattices. In particular, control over the oxygen degree of freedom in dedicated heterostructures is not restricted to the detailed sample preparation process, see [68] for an impressive example, but further relates to intrinsic properties of specific interfaces.

4. Summary

Our combined study of YBCO/PCMO multilayers reveals detailed information about their atomic and electronic interfacial structure and the related superconducting transport properties. We found evidence for interfacial electron transfer from PCMO to YBCO and further intrinsic underdoping of the cuprate on a 3 nm scale by oxygen depletion, presumably as an adaptation to a compressively strained environment. The corresponding reduction in the critical temperature of superconductivity proves to be stronger than that in the case of primarily magnetic impacts reported for superlattices with ferromagnetic manganites.

Acknowledgments

JN and CJ acknowledge funding by Deutsche Forschungsgemeinschaft under SFB602. Work at Brookhaven was supported by the US Department of Energy, Office of Basic Energy Science, Division of Materials Science and Engineering, under contract no. DE-AC02-98CH10886.

References

[1] Borisevich A Y *et al* 2010 Suppression of octahedral tilts and associated changes in electronic properties at epitaxial oxide heterostructure interfaces *Phys. Rev. Lett.* **105** 087204
[2] He J, Borisevich A, Kalinin S V, Pennycook S J and Pantelides S T 2010 Control of octahedral tilts and magnetic properties of perovskite oxide heterostructures by substrate symmetry *Phys. Rev. Lett.* **105** 227203
[3] Nakagawa N, Hwang H Y and Muller D A 2006 Why some interfaces cannot be sharp? *Nature Mater.* **5** 204
[4] Zhong Z, Xu P X and Kelly P J 2010 Polarity-induced oxygen vacancies at $LaAlO_3/SrTiO_3$ interfaces *Phys. Rev.* B **82** 165127
[5] Ohtomo A and Hwang H Y 2004 A high-mobility electron gas at the $LaAlO_3/SrTiO_3$ heterointerface *Nature* **427** 423
[6] Haeni J H *et al* 2004 Room-temperature ferroelectricity in strained $SrTiO_3$ *Nature* **430** 758
[7] Yu P *et al* 2010 Interface ferromagnetism and orbital reconstruction in $BiFeO_3$–$La_{0.7}Sr_{0.3}MnO_3$ heterostructures *Phys. Rev. Lett.* **105** 027201
[8] Okamoto S and Millis A J 2004 Electronic reconstruction at an interface between a Mott insulator and a band insulator *Nature* **428** 630
[9] Yunoki S, Moreo A, Dagotto E, Okamoto S, Kancharla S S and Fujimori A 2007 Electron doping of cuprates via interfaces with manganites *Phys. Rev.* B **76** 064532
[10] Hwang H Y, Iwasa Y, Kawasaki M, Keimer B, Nagaosa N and Tokura Y 2012 Emergent phenomena at oxide interfaces *Nature Mater.* **11** 103
[11] Li Q *et al* 1990 Interlayer coupling effect in high-T_c superconductors probed by $YBa_2Cu_3O_{7-x}/PrBa_2Cu_3O_{7-x}$ superlattices *Phys. Rev. Lett.* **64** 3086
[12] Varela M, Sefrioui Z, Arias D, Navacerrada M A, Lucía M, López de la Torre M A, León C, Loos G D, Sánchez-Quesada F and Santamaría J 1999 Intracell changes in epitaxially strained $YBa_2Cu_3O_{7-x}$ ultrathin layers in $YBa_2Cu_3O_{7-x}/PrBa_2Cu_3O_7$ superlattices *Phys. Rev. Lett.* **83** 3936
[13] Varela M, Arias D, Sefrioui Z, León C, Ballesteros C and Santamaría J 2000 Epitaxial mismatch strain in $YBa_2Cu_3O_{7-\delta}/PrBa_2Cu_3O_7$ superlattices *Phys. Rev.* B **62** 12509
[14] Goldman A M, Vas'ko V, Kraus P, Nikolaev K and Larkin V A 1999 Cuprate/manganite heterostructures *J. Magn. Magn. Mater.* **200** 69
[15] Soltan S, Albrecht J and Habermeier H-U 2004 Ferromagnetic/superconducting bilayer structure: a model system for spin diffusion length estimation *Phys. Rev.* B **70** 144517

[16] Stahn J *et al* 2005 Magnetic proximity effect in perovskite superconductor/ferromagnet multilayers *Phys. Rev.* B **71** 140509
[17] Hoffmann A, te Velthuis S G E, Sefrioui Z, Santamaría J, Fitzsimmons M R, Park S and Varela M 2005 Suppressed magnetization in $La_{0.7}Ca_{0.3}MnO_3/YBa_2Cu_3O_{7-\delta}$ superlattices *Phys. Rev.* B **72** 140407
[18] Nemes N M *et al* 2008 Origin of the inverse spin-switch behavior in manganite/cuprate/manganite trilayers *Phys. Rev.* B **78** 094515
[19] Dybko K, Werner-Malento K, Sawicki M and Przyslupski P 2009 Enhancement of the superconducting transition temperature by an external magnetic field parallel to the plane of $La_{0.7}Sr_{0.3}MnO_3/YBa_2Cu_3O_7/La_{0.7}Sr_{0.3}MnO_3$ trilayers *Europhys. Lett.* **85** 57010
[20] Salafranca J and Okamoto S 2010 Unconventional proximity effect and inverse spin-switch behavior in a model manganite–cuprate–manganite trilayer system *Phys. Rev. Lett.* **105** 256804
[21] Visani C *et al* 2011 Symmetrical interfacial reconstruction and magnetism in $La_{0.7}Ca_{0.3}MnO_3/YBa_2Cu_3O_7/La_{0.7}Ca_{0.3}MnO_3$ heterostructures *Phys. Rev.* B **84** 060405
[22] Inada H, Wu L, Wall J, Su D and Zhu Y 2009 Performance and image analysis of the aberration-corrected Hitachi HD-2700C STEM *J. Electron. Microsc.* **58** 111
[23] Fu L F, Browning N D, Ramadan W, Ogale S B, Kundaliya D C and Venkatesan T 2007 Interface and defect structures in $YBa_2Cu_3O_{7-\delta}$ and Nb: $SrTiO_3$ heterojunction *J. Phys. D: Appl. Phys.* **40** 187
[24] Haage T, Zegenhagen J, Li J Q, Habermeier H-U, Cardona M, Jooss Ch, Warthmann R, Forkl A and Kronmüller H 1997 Transport properties and flux pinning by self-organization in $YBa_2Cu_3O_{7-\delta}$ films on vicinal $SrTiO_3$(001) *Phys. Rev.* B **56** 8404
[25] Davoli I, Marcelli A, Bianconi A, Tomellini M and Fanfoni M 1986 Multielectron configurations in the x-ray-absorption near-edge structure of NiO at the oxygen K threshold *Phys. Rev.* B **33** 2979
[26] Abbate M *et al* 1992 Controlled-valence properties of $La_{1-x}Sr_xFeO_3$ and $La_{1-x}Sr_xMnO_3$ studied by soft-x-ray absorption spectroscopy *Phys. Rev.* B **46** 4511
[27] Nücker N, Fink J, Fuggle J C, Durham P J and Temmerman W M 1988 Evidence for holes on oxygen sites in the high-T_c superconductors $La_{2-x}Sr_xCuO_4$ and $YBa_2Cu_3O_{7-y}$ *Phys. Rev.* B **37** 5158
[28] Kourkoutis L F, Xin H L, Higuchi T, Hotta Y, Lee J H, Hikita Y, Schlom D G, Hwang H Y and Muller D A 2010 Atomic-resolution spectroscopic imaging of oxide interfaces *Phil. Mag.* **90** 4731
[29] de Groot F M F, Grioni M, Fuggle J C, Ghijsen J, Sawatzky G A and Petersen H 1989 Oxygen 1s x-ray-absorption edges of transition-metal oxides *Phys. Rev.* B **40** 5715
[30] Kurata H and Colliex C 1993 Electron-energy-loss core-edge structures in manganese oxides *Phys. Rev.* B **48** 2102
[31] Browning N D, Yuan J and Brown L M 1992 Determination of the local oxygen stoichiometry in $YBa_2Cu_3O_{7-\delta}$ by electron energy loss spectroscopy in the scanning transmission electron microscope *Physica* C **202** 12
[32] Browning N D, Chisholm M F, Pennycook S J, Norton D P and Lowndes D H 1993 Correlation between hole depletion and atomic structure at high angle grain boundaries in $YBa_2Cu_3O_{7-\delta}$ *Physica* C **212** 185
[33] Varela M, Oxley M P, Luo W, Tao J, Watanabe M, Lupini A R, Pantelides S T and Pennycook S J 2009 Atomic-resolution imaging of oxidation states in manganites *Phys. Rev.* B **79** 085117
[34] de Groot F 2005 Multiplet effects in x-ray spectroscopy *Coord. Chem. Rev.* **249** 31
[35] Rask J H, Miner B A and Buseck P R 1987 Determination of manganese oxidation states in solids by electron energy-loss spectroscopy *Ultramicroscopy* **21** 321
[36] Riedl T, Gemming T, Gruner W, Acker J and Wetzig K 2007 Determination of manganese valency in $La_{1-x}Sr_xMnO_3$ using ELNES in the (S)TEM *Micron* **38** 224
[37] Zhu Y, Zuo J M, Moodenbaugh A R and Suenaga M 1994 Grain-boundary constraint and oxygen deficiency in $YBa_2Cu_3O_{7-\delta}$: application of the coincidence site lattice model to a non-cubic system *Phil. Mag.* A **70** 969
[38] Reagor D W, Lee S Y, Li Y and Jia Q X 2004 Work function of the mixed-valent manganese perovskites *J. Appl. Phys.* **95** 7971

[39] van Zalk Mand Brinkman A, Aarts J and Hilgenkamp H 2010 Interface resistance of $YBa_2Cu_3O_{7-\delta}$/$La_{0.67}Sr_{0.33}MnO_3$ ramp-type contacts *Phys. Rev.* B **82** 134513
[40] Anderson R L 1962 Experiments on Ge–GaAs heterojunctions *Solid State Electron.* **5** 341
[41] Testardi L R, Moulton W G, Mathias H, Ng H K and Rey C M 1988 Large static dielectric constant in the high-temperature phase of polycrystalline $YBa_2Cu_3O_x$ *Phys. Rev.* B **37** 2324
[42] Biskup N, de Andres A, Martinez J L and Perca C 2005 Origin of the colossal dielectric response of $Pr_{0.6}Ca_{0.4}MnO_3$ *Phys. Rev.* B **72** 024115
[43] Greaves C and Slater P R 1989 The structural effects of Na and Ca substitutions on the Y site in $YBa_2Cu_3O_{7-x}$ *Supercond. Sci. Technol.* **2** 5
[44] Yoshizawa H, Kawano H, Tomioka Y and Tokura Y 1995 Neutron-diffraction study of the magnetic-field-induced metal–insulator transition in $Pr_{0.7}Ca_{0.3}MnO_3$ *Phys. Rev.* B **52** R13145
[45] Tomioka Y, Asamitsu A, Kuwahara H, Moritomo Y and Tokura Y 1996 Magnetic-field-induced metal–insulator phenomena in $Pr_{1-x}Ca_xMnO_3$ with controlled charge-ordering instability *Phys. Rev.* B **53** R1689
[46] Deac I G, Mitchell J F and Schiffer P 2001 Phase separation and low-field bulk magnetic properties of $Pr_{0.7}Ca_{0.3}MnO_3$ *Phys. Rev.* B **63** 172408
[47] Niebieskikwiat D, Hueso L E, Borchers J A, Mathur N D and Salamon M B 2007 Nanoscale magnetic structure of ferromagnet/antiferromagnet manganite multilayers *Phys. Rev. Lett.* **99** 247207
[48] Ziese M, Vrejoiu I, Pippel E, Nikulina E and Hesse D 2011 Magnetic properties of $Pr_{0.7}Ca_{0.3}MnO_3/SrRuO_3$ superlattices *Appl. Phys. Lett.* **98** 132504
[49] Sefrioui Z, Arias D, Pena V, Villegas J E, Varela M, Prieto P, León C, Martinez J L and Santamaría J 2003 Ferromagnetic/superconducting proximity effect in $La_{0.7}Ca_{0.3}MnO_3/YBa_2Cu_3O_{7-\delta}$ superlattices *Phys. Rev.* B **67** 214511
[50] Bibes M, Balcells Ll, Valencia S, Fontcuberta J, Wojcik M, Jedryka E and Nadolski S 2001 Nanoscale multiphase separation at $La_{2/3}Ca_{1/3}MnO_3/SrTiO_3$ interfaces *Phys. Rev. Lett.* **87** 067210
[51] Borges R P, Guichard W, Lunney J G, Coey J M D and Ott F 2001 Magnetic and electric 'dead' layers in $La_{0.7}Sr_{0.3}MnO_3$ thin films *J. Appl. Phys.* **89** 3868
[52] Angeloni M, Balestrino G, Boggio N G, Medaglia P G, Orgiani P and Tebano A 2004 Suppression of the metal–insulator transition temperature in thin $La_{0.7}Sr_{0.3}MnO_3$ films *J. Appl. Phys.* **96** 6387
[53] Huijben M, Martin L W, Chu Y-H, Holcomb M B, Yu P, Rijnders G, Blank D H A and Ramesh R 2008 Critical thickness and orbital ordering in ultrathin $La_{0.7}Sr_{0.3}MnO_3$ films *Phys. Rev.* B **78** 094413
[54] Cava R J, Batlogg B, Chen C H, Rietman E A, Zahurak S M and Werder D 1987 Single-phase 60-K bulk superconductor in annealed $Ba_2YCu_30_{7-\delta}$ ($0.3 < \delta < 0.4$) with correlated oxygen vacancies in the Cu–O chains *Phys. Rev.* B **36** 5719
[55] Rothman S J, Routbort J L, Welp U and Baker J E 1991 Anisotropy of oxygen tracer diffusion in single-crystal $YBa_2Cu_3O_{7-\delta}$ *Phys. Rev.* B **44** 2326
[56] De Souza R A and Kilner J A 1998 Oxygen transport in $La_{1-x}Sr_xMn_{1-y}Co_yO_{3\pm\delta}$ perovskites: I. Oxygen tracer diffusion *Solid State Ion.* **106** 175
[57] Przyslupski P, Komissarov I, Paszkowicz W, Dluzewski P, Minikayev R and Sawicki M 2004 Magnetic properties of $La_{0.67}Sr_{0.33}MnO_3/YBa_2Cu_3O_7$ superlattices *Phys. Rev.* B **69** 134428
[58] Char K, Antognazza L and Geballe T H 1993 Study of interface resistances in epitaxial $YBa_2Cu_3O_{7-x}$/barrier/$YBa_2Cu_3O_{7-x}$ junctions *Appl. Phys. Lett.* **63** 2420
[59] Hÿtch M J, Snoeck E and Kilaas R 1998 Quantitative measurement of displacement and strain fields from HREM micrographs *Ultramicroscopy* **74** 131
[60] Cava R J, Batlogg B, Rabe K M, Rietman E A, Gallagher P K and Rupp L W Jr 1988 Structural anomalies at the disappearance of superconductivity in $Ba_2YCu_3O_{7-\delta}$: evidence for charge transfer from chains to planes *Physica* C **156** 523
[61] Kramer T 2010 Mechanische Spannungen und Dehnungen in dünnen $Pr_{0.64}Ca_{0.36}MnO_3$ Filmen *Diploma Thesis* University of Goettingen

[62] Roa J J, Capdevila X G, Martínez M, Espiell F and Segarra M 2007 Nanohardness and Young's modulus of YBCO samples textured by the Bridgman technique *Nanotechnology* **18** 385701

[63] Hibble S J, Cooper S P, Hannon A C, Fawcett I D and Greenblatt M 1999 Local distortions in the colossal magnetoresistive manganates $La_{0.70}Ca_{0.30}MnO_3$, $La_{0.80}Ca_{0.20}MnO_3$ and $La_{0.70}Sr_{0.30}MnO_3$ revealed by total neutron diffraction *J. Phys.: Condens. Matter* **11** 9221

[64] López-Morales M E, Ríos-Jara D, Tagüea J, Escudero R, La Placa S, Bezinge A, Lee V Y, Engler E M and Grant P M 1990 Role of oxygen in $PrBa_2Cu_3O_{7-y}$: effect on structural and physical properties *Phys. Rev.* B **41** 6655

[65] Skakle J M S 1998 Crystal chemical substitutions and doping of $YBa_2Cu_3O_x$ and related superconductors *Mater. Sci. Eng.* R **23** 1

[66] Klie R F, Buban J P, Varela M, Franceschetti A, Jooss C, Zhu Y, Browning N D, Pantelides S T and Pennycook S J 2005 Enhanced current transport at grain boundaries in high-T_c superconductors *Nature* **435** 475

[67] Berenov A V, Foltyn S R, Schneider C W, Warburton P A and MacManus-Driscoll J L 2003 Determination of Ca diffusion in YBCO films by secondary ion mass spectroscopy *Solid State Ion.* **164** 149

[68] Ferguson J D, Kim Y, Kourkoutis L F, Vodnick A, Woll A R, Muller D A and Brock J D 2011 Epitaxial oxygen getter for a brownmillerite phase transformation in manganite films *Adv. Mater.* **23** 1226